

Beamformer With Constant-Gm Vector Modulators and Its Spatial Intermodulation Distortion

Michiel C. M. Soer, Eric A. M. Klumperink, *Senior Member, IEEE*, Dirk-Jan van den Broek, Bram Nauta, *Fellow, IEEE*, and Frank E. van Vliet, *Senior Member, IEEE*

Abstract—Spatial interference rejection in analog adaptive beamforming receivers can improve the distortion performance of the circuits following the beamforming network, but is susceptible to the nonlinearity of the beamforming network itself. This paper presents an analysis of intermodulation product cancellation in analog active phased array receivers and verifies the distortion improvement in a four-element adaptive beamforming receiver for low-power applications in the 1.0–2.5-GHz frequency band. In this architecture, a constant-Gm vector modulator is proposed that produces an accurate equidistance square constellation, leading to a sliced frontend design that is duplicated for each antenna element. By moving the transconductances to RF, a fourfold reduction in power is achieved, while simultaneously providing input impedance matching. The 65-nm implementation consumes between 6.5 and 9 mW per antenna element and shows a +1 to +20 dBm in-band and out-of-beam third-order intercept point due to intermodulation distortion reduction.

Index Terms—Analog beamforming, compression point (CP), intercept point, interference nulling, mixer, phase shifter, phased array, receiver, spatial filtering, switched capacitor, vector modulator.

I. INTRODUCTION

IN BEAMFORMING phased-array receivers, the aim is to combine signals from multiple antennas such that sensitivity is improved and interferers are rejected in the spatial domain [1]–[4]. As is sketched schematically in Fig. 1, an interference cancelling beamforming receiver aims to maximize the received amplitude of the desired signals, while simultaneously minimizing the amplitude of one or multiple interferers. This is achieved by amplitude and phase weighting of the received signals from multiple antennas, usually spaced half the carrier wavelength apart, and summing into a common output signal [5].

Increasing the number of antennas improves the sensitivity at the expense of increased power consumption due to the

Manuscript received May 9, 2016; revised July 18, 2016, September 8, 2016, and November 22, 2016; accepted December 3, 2016. Date of publication January 4, 2017; date of current version March 3, 2017. This paper was approved by Associate Editor Hossein Hashemi. This work was supported by the Dutch Government through the Sensor Technology Applied in Reconfigurable systems for sustainable Security project.

M. C. M. Soer was with the IC-Design Group, CTIT, University of Twente, 7500 AE Enschede, The Netherlands. He is now with Spark Microsystems, Montreal, QC H3A 0B4, Canada (e-mail: m.c.m.soer@alumnus.utwente.nl).

E. A. M. Klumperink, D. J. van den Broek, and B. Nauta are with the IC-Design Group, CTIT, University of Twente, 7500 AE Enschede, The Netherlands (e-mail: e.a.m.klumperink@utwente.nl; j.d.a.vandenbroek@utwente.nl; b.nauta@utwente.nl).

F. E. van Vliet is with TNO, 2509 JG The Hague, The Netherlands, and also with the IC-Design Group, CTIT, University of Twente, 7500 AE Enschede, The Netherlands (e-mail: frank.vanyliet@tno.nl).

Color versions of one or more of the figures in this paper are available online at <http://ieeexplore.ieee.org>.

Digital Object Identifier 10.1109/JSSC.2016.2639545

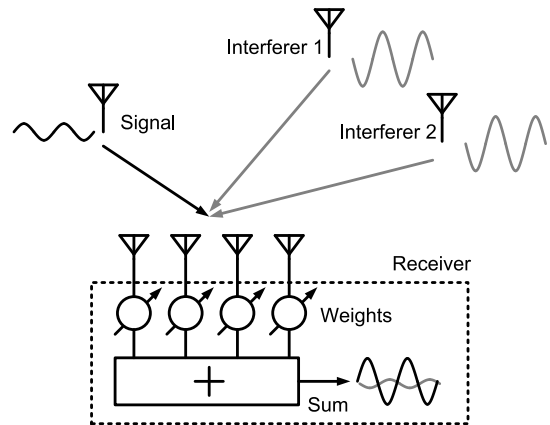


Fig. 1. Principle of a beamforming receiver for sensitivity improvement and interferer suppression.

multiple receiver frontends. A power-efficient frontend is thus required, and the signals from the multiple frontends should be combined into a beamformed signal as early in the receiver chain as possible. On the other hand, interferers are suppressed by spatial filtering after the summing node, placing stringent linearity requirements on the receiver frontends. A tradeoff between low power consumption and distortion performance is therefore fundamental in the frontend design.

Good linearity can be achieved by adopting a passive switched capacitor architecture for the antenna elements and summing node [6]–[8]. This comes at the cost of increased noise figure and clock power consumption. Recently, a gain-boosted mixer-first receiver frontend was proposed with impedance-translated spatial notch at the antenna input and digital beamforming, greatly boosting out-of-band interferer rejection [9]. An analog beamformer with active preamplification and passive mixer/phase shifter and summing node was presented earlier [10] and demonstrated reduced power consumption at the expense of in-band and in-beam linearity performance.

In phased array receivers, the power consumption of an antenna element should be kept as low as possible, since the elements are duplicated several times to form the full array. This conflicts with the demand for good linearity of the receiver frontend to withstand interferers before spatial filtering occurs, which in general raises the power consumption. A combination of a low-power beamforming architecture with adaptive interference nulling could potentially give the best tradeoff. In this case, the nulling beamforming algorithm has to operate on the intermodulation products created by the receiver

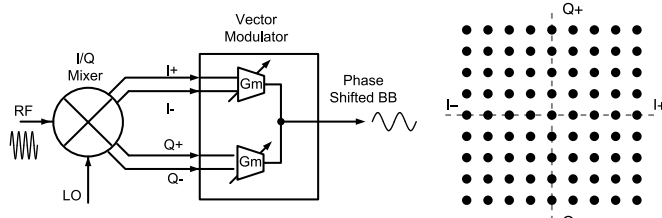


Fig. 2. Cartesian baseband vector modulator block diagram and phase shift constellation.

frontend instead of the fundamental signals themselves. The phases of these intermodulation products across antenna elements are expected to behave differently from conventional beamforming, asking for an updated analysis approach.

In this paper, we therefore provide a theoretical basis for the propagation and beamforming of intermodulation products in active phased array receivers and demonstrate the achievable linearity enhancements in measurements. This paper specifically targets beamforming for interference rejection in the low-gigahertz bands, for instance, in the 2.4 GHz band, which is becoming very crowded. More information of interference mitigation by integrated MIMO system can, for instance, be found in [11]. To this end, this paper first expands on the analysis and design of the low-power beamforming architecture published earlier [10], by analyzing the constant-Gm vector modulation topology in Section II and the low-power implementation of the beamforming receiver in Section III. Next, Section IV focuses in detail on the intermodulation distortion performance in active phased arrays and proposes a theoretical model. Single-element and array measurement results are reported in Section V to verify the linearity analysis, followed by conclusions in Section VI.

II. VECTOR MODULATOR ARCHITECTURES

A. Cartesian Vector Modulator

The vector modulator is a combined phase shifter/amplitude modulator that in general depends on adding multiple copies of the input signal with different phase shifts and amplitude gains [1], [2], [12], [13]. In the phasor domain, each copy is represented by a vector whose length indicates the signal amplitude gain and whose orientation indicates the signal phase shift. We can see that the combination of different vectors can lead to a final vector with arbitrary amplitude gain and phase shift, i.e., summing signal copies with different amplitude gains and phase shifts results in a summed signal that has arbitrary amplitude gain and phase shift. Vector modulator architectures differ in the way in which different phase shifts are generated and how amplitude gains are applied.

In a Cartesian vector modulator, a set of four basis signals having 0°, 90°, 180°, and 270° phases are first generated. A convenient way of generating these phases in many radio architectures is to use the in-phase (I) and quadrature (Q) outputs of a mixer, as well as their negative counterparts in a balanced structure, as is indicated in Fig. 2.

As summing is easy in the current domain and many I/Q mixers produce output voltages, variable transconductors are

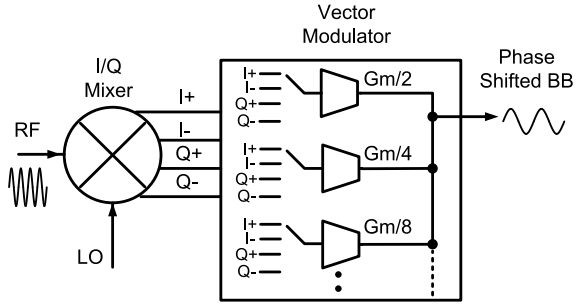


Fig. 3. Constant-Gm baseband vector modulator block diagram.

used to both convert into the current domain and scale the I and Q signals and sum into a common node. In order to reach all four quadrants of the phase shifter constellation (and hence cover a full 360° phase shift), it is necessary to have opposite phase I and Q signals available. In baseband zero-IF architectures, differential signaling is implemented to reject common-mode noise and disturbances, providing the required balanced signals. Also note that in order to preserve this rejection and to facilitate demodulation, it is required to generate a phase-shifted four-phase output that is again differential and I/Q . Therefore, the hardware in a baseband Cartesian vector modulator is replicated four times.

Note that the *phase shifter* constellation is different from the *modulation* constellation of the signal itself. Each point in the phase shifter constellation represents an amplitude and phase adjustment that the vector modulator is capable of, represented as a phasor. Whereas the modulation changes its constellation point for each symbol, the phase shifter constellation point is constant and changes only when the array is pointed to a different position. The modulation constellation of the signal is thus preserved while passing through the vector modulator, apart from the scaling and rotation of the entire signal constellation corresponding to the applied amplitude and phase adjustment.

B. Constant-Gm Vector Modulator

From the principle of the Cartesian vector modulator in Fig. 2, we can observe that each constellation point requires different lengths of vectors and that the sum of their lengths is also variable. In implementing this architecture, care must therefore be taken that the variable amount of transconductance does not introduce phase and gain errors in the constellation. Moreover, good isolation between the output and the input of the variable transconductance is required.

Instead, in this paper, we propose a vector modulator architecture that always uses the same total amount of transconductance to produce a constellation point. The constant-Gm circuit architecture is shown in Fig. 3 and consists of a mixer as a I/Q generator, a fixed bank of N binary scaled transconductances whose currents are summed into the output, and a set of reconfiguration switches at the transconductor inputs. These switches allow each transconductor to pick one of the four mixer phases, which effectively rotates its phase by 0°, 90°, 180°, or 270°.

The resulting constellation (shown in Fig. 4 for $N = 1$, $N = 2$ and $N = 3$) is square with equidistance points, but

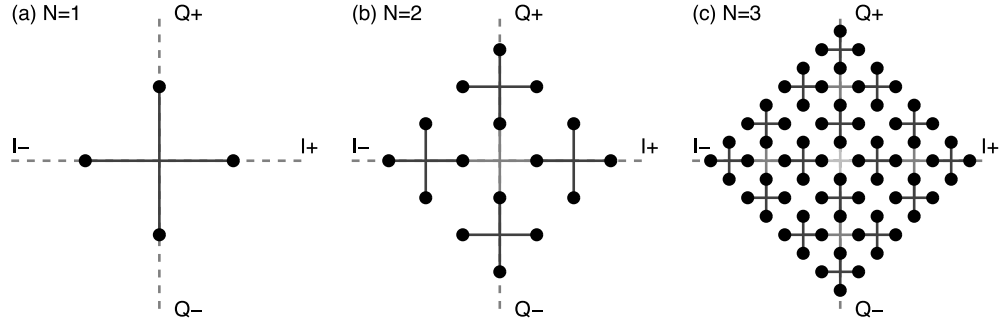


Fig. 4. Constant-Gm phase shift constellation for (a) $N = 1$, (b) $N = 2$, and (c) $N = 3$.

rotated 45° with respect to the Cartesian vector modulator. It can therefore produce the same phase shifts and amplitudes with similar quantization errors. The advantage of the constant-Gm vector modulator is that for any constellation point, the same number of transconductances is enabled. This translates into equal loading of all circuit nodes (including the RF input node), and therefore, a higher precision in the constellation. Moreover, the total amount of transconductance for producing the same maximum output current is reduced by $\sqrt{2}$. In a Cartesian vector modulator, the transconductors are split by half on the real and imaginary axes, and a summation leads to a maximum of $1/\sqrt{2}$ times the total transconductance. In contrast, the transconductances in the constant-Gm vector modulator can sum up in-phase to the full total transconductance.

The constellation can be expanded by increasing N , i.e., by adding smaller binary scaled transconductances. The achievable phase resolution is limited by several factors. The I/Q phase error of the local oscillator (LO) clock generation can deform the constellation to a trapezoid shape, in a similar way to I/Q phase errors in image-reject receivers. Furthermore, the mismatch between the transconductances generates randomly distributed phase and gain errors, which can limit the resolution.

The mapping of desired phase shift and amplitude scaling is achieved by picking the nearest possible constellation point, and therefore, more transconductance quantization steps result in more vector modulator accuracy [4]. The maximum amplitude of the vector modulator is determined by the largest circle that can be drawn inside the boundaries of the constellation. Constellation points outside of this circle (in the corners) are therefore not usable.

The resolution of the quantized phase steps can be estimated by the realization that the shortest distance between two constellation points is approximately mapped to an arc that is a fraction of a circle with maximum radius that fits into the square constellation

$$\text{phase points} \approx 2\pi \cdot 0.9 \cdot L \quad (1)$$

where the factor of 0.9 is a fitting factor to compensate for the curvature of the arc and L is the number of points along one axis in the square constellation. The number of phase points has to be rounded to the closest multiple of 4 to obtain a symmetric constellation. For example, in a 16×16 square

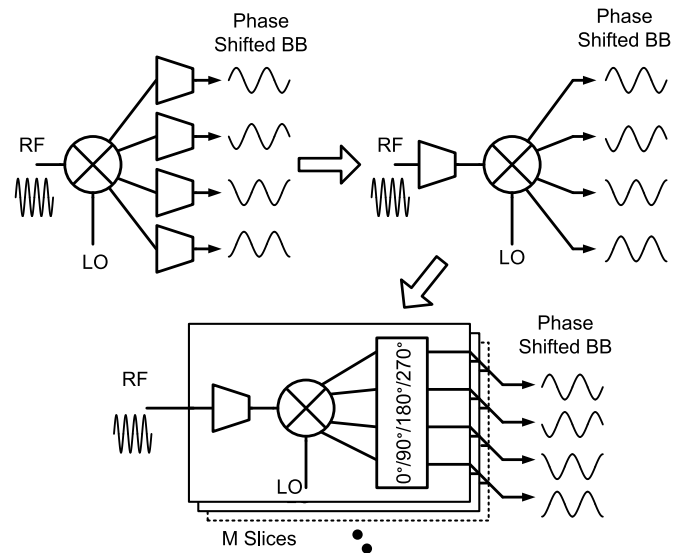


Fig. 5. Transformation of the transconductance from baseband to RF for a passive mixer with nonoverlapping clock phases and subsequent slicing into a constant-Gm vector modulator.

constellation, the number of quantized phase points will be 44. An estimate for the depth of a null with respect to the main beam QL is given in decibels by [4]

$$QL \approx 6 \cdot \log_2(K) - 4 \quad (2)$$

where K is the number of phase steps in the phase shifter. This results in a rejection of 29 dB for 44 phase steps.

The constant-Gm vector modulator as depicted in Fig. 3 has the drawback that four duplicate sets of transconductors are required for the four mixer phases. We can, however, share the transconductors between the mixer phases in the case of a passive current mixer with nonoverlapping clock phases (less than 25% duty cycle in this case). Since the current in such a mixer is steered toward one output at a time, the transconductors can be shared and thus moved to the RF domain. This baseband to RF transformation is conceptually depicted in Fig. 5. Operation as a constant-Gm vector modulator is enabled by subdividing both the mixer and transconductor into multiple identical slices. The reconfiguration switches are in the baseband domain and essentially perform a 0° , 90° , 180° , or 270° phase shift for each slice. In general, for a constant-Gm architecture with N binary scaled groups, the number of

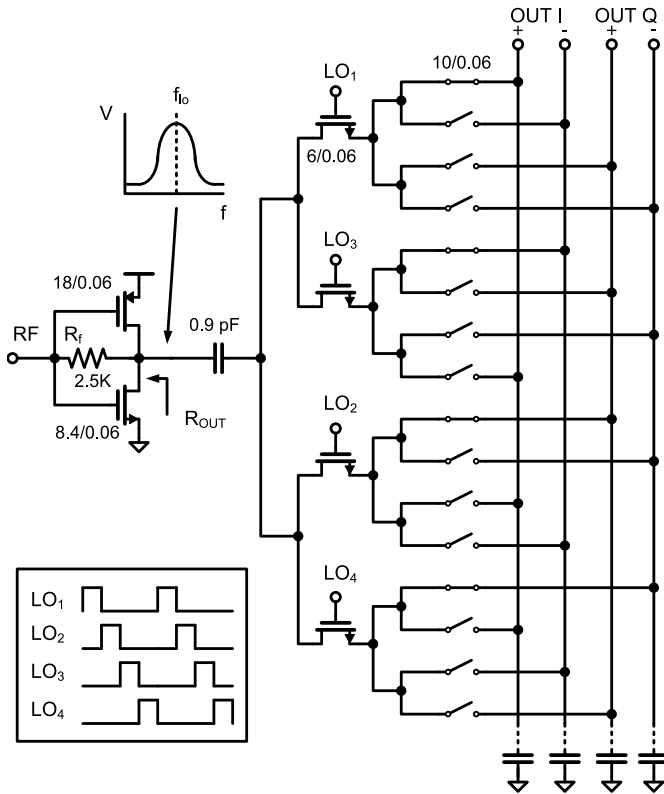


Fig. 6. Unit slice of the receiver frontend.

identical slices M needed for the vector modulator is equal to

$$M = 2^N - 1. \quad (3)$$

For a constant-Gm architecture with N binary scaled transconductors, a $2^N \times 2^N$ constellation is created.

Changing the order from mixer–switches–transconductors (Fig. 3) to transconductors–mixer–switches thus enables a four times reduction in the number of transconductors, with an associated four times reduction in power consumption.

III. LOW-POWER CIRCUIT IMPLEMENTATION

A. Low-Power Beamforming Frontend Topology

In order to implement the constant-Gm vector modulator, three elements are required: 1) a transconductor; 2) an I/Q mixer; and 3) reconfiguration switches. The low-power implementation consists of a four-phase 25% duty cycle passive RC mixer for generating differential I/Q , as shown in Fig. 6. This mixer consumes no static power and has a low conversion loss and a low noise figure for the case where the RC product of the resistance driving the mixer (R_{OUT}) and load capacitance (C_{BB}) is larger than the switch-on time [14]. The theoretical minimum conversion loss and noise figure for 25% duty cycle is 0.9 dB, with additional noise from the switch resistances [14]. The switching mixer folds back harmonic images around three times and five times the LO frequency with the rejections of 10 and 14 dB respectively, as well as higher harmonics, so an additional RF bandpass filter will be required [15].

Adding reconfiguration switches after each mixer to steer the current of each slice to one of the four outputs completes

the components for the vector modulator. Their on-resistance can be made low by sizing the transistors large, as their capacitance can be absorbed into the baseband capacitors. The baseband bandwidth can be made reconfigurable by implementing the baseband capacitors as a variable capacitor bank, without affecting the vector modulator constellation, at no additional power consumption.

The vector modulator transconductance at RF acts as a low-noise amplifier (LNA) and provides input matching at the RF input port. In this design, a shunt resistor feedback inverter amplifier operating in moderate inversion is chosen because of its high power efficiency. The inverter reuses current in the NMOS and the PMOS, which both contribute to the total transconductance. The shunt feedback resistor provides a low noise and low power impedance match due to the Miller effect caused by the voltage gain between the input and the output of the amplifier [16], [17]. The output impedance looking into the inverter structure is calculated as

$$R_{\text{OUT}} = R_{\text{ds},N} // R_{\text{ds},P} // \frac{R_s + R_f}{1 + (\text{Gm}_N + \text{Gm}_P)R_s} \quad (4)$$

where $R_{\text{ds},N}$ and $R_{\text{ds},P}$ are the output conductances of the inverter NMOS and PMOS, respectively, Gm_N and Gm_P are the NMOS and PMOS transconductances, respectively, R_s is the source resistance driving the RF port, and R_f is the shunt feedback resistance.

By ac coupling the receiver at RF and biasing the sources and drains of the mixer switches at ground potential, the inverters of the clock tree can directly drive the gates of the mixer switches with large overdrive. The added benefit of RF ac coupling is the blocking of second-order intermodulation (IM2) products generated by the LNA inverter, which boosts narrowband second-order intercept point performance, as well as filtering of the inverter 1/f noise. The ac coupling capacitor is implemented with a metal–insulator–metal capacitor for minimum parasitic capacitance to ground (1% of the capacitance value). The combined parasitic capacitance to ground of the LNA, ac coupling capacitor, and mixer switches forms a pole with the output impedance of the LNA and therefore limits the RF bandwidth of the system.

Because a minimum-gate-length inverter is used as the LNA, its intrinsic gain is limited to 7.5 and noise contribution due to the output impedance of the LNA and the mixer switches raises the noise figure of a single element to about 6 dB in simulation. Alternatively, a larger than minimum gate length can result in better gain, linearity, and noise figure at the expense of lower RF bandwidth.

This receiver slice is expanded into the full beamforming receiver with vector modulation by copying the unit slice multiple times and connecting the baseband capacitance nodes together, which is shown schematically in Fig. 7. The currents of the antenna elements are summed into the summing node and filtered by the common baseband capacitances.

In the implemented $N = 4$ design with a 16×16 constellation, a total of 15 slices per element are needed, with each slice providing 1/15th of the input match. This structure is again multiplied for the number of antenna elements that is needed. In contrast to the Cartesian vector modulator, there

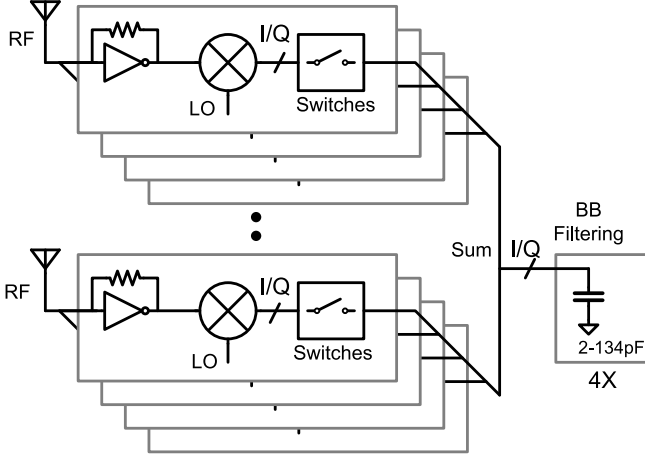


Fig. 7. Receiver frontend with constant-Gm vector modulation.

are no variable transconductances but only a rerouting of mixer current. Therefore, the constant-Gm topology provides a constant impedance match and also a constant mixer baseband bandwidth over all vector modulator codes.

B. Mixer Transformation Properties

One important aspect of the passive mixer is its lack of isolation from output to input. Rather than an undesirable property, this fact is utilized in this design to improve the receiver's robustness to large interferers in the frequency and spatial domain [7].

The important observation to note is that the voltage swing on the mixer RF node is a translation of the baseband voltage swings [18]. A lowering of the baseband voltage swing therefore results in lowering of the RF voltage swing.

In the frequency domain, this property expresses itself in the low-pass filtering by the baseband capacitors. The -3 dB baseband bandwidth of the passive mixer is determined by the output impedance of the inverter structure including feedback resistance, together with the baseband capacitors (assuming that switch resistance is negligible compared with the inverter output resistance)

$$\text{BW} = \frac{1}{2\pi \cdot 4 \cdot R_{\text{out}} C_{\text{BB}}}. \quad (5)$$

Intuitively, the factor of 4 can be understood as relating to duty cycle: each capacitor is only charged 1/4 of the period. In the stop band of this low-pass filter, the voltage swing on the baseband capacitor as well as the mixer RF node is reduced. Effectively, the low-pass filter at baseband is translated into a bandpass filter at RF centered around the clock frequency [7], [19], [20]. The reduced out-of-band voltage swing at the inverter output increases its out-of-band compression point (CP) as well as third-order intercept points due to output conductance nonlinearity.

This concept can be extended to the beamforming pattern of the array in the spatial domain. For signals coming from the directions for which the beamforming algorithm maximizes the signal amplitude, the currents from the array elements are in phase and sum up coherently into a larger current, which

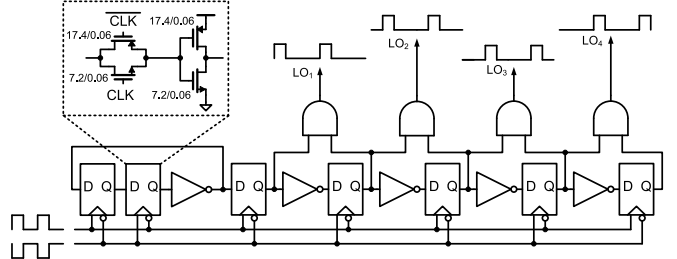


Fig. 8. Clock generation block diagram.

results in a large voltage swing on the baseband capacitors. For cancelled signals, the element currents destructively sum into a small current and hence a lowered baseband voltage swing. Since this reduced voltage swing is transformed into the RF node, the out-of-beam CP and weak nonlinearity of the inverters are also improved.

C. Clock Generation

An accurate four-phase 25% duty cycle clock is required to drive the mixer switches in the vector modulator. Phase errors between clock phases are transferred to the phases of the rotated vector in the modulator, resulting in gain and phase errors after summation. As a result, the square constellation may become trapezoid, a property that is known from image-reject receiver architectures.

The clock generation is performed on-chip in a clock divider architecture, as shown in Fig. 8, with a differential external clock as a reference. The first part of the clock generation performs a divide-by-two with a looped flip-flop, in order to divide down the reference clock and produce enough clock edges to select for the four clock phases. Next, a shift register generates the four phases, but with a 50% duty cycle. Therefore, AND gates combine pairs of shift register outputs together to produce 25% duty cycle clock signals.

The balance of the differential reference clock is of importance, as the edges of half the output phases originate from the positive reference, while the edges of the other half originate from the negative reference. In other words, a phase imbalance in the reference clock is transferred to an *I/Q* imbalance in the output phases. Therefore, the reference is first amplified with current mode logic buffers whose common mode rejection reduces common-mode components in the clock and therefore the imbalance. These buffers also serve the purpose of boosting the reference clock amplitude to a square waveform. In simulation, the RMS phase imbalance is found to be 0.7° .

IV. INTERMODULATION PRODUCTS IN ACTIVE BEAMFORMING ARRAYS

A. Frontend Linearity Model

Fig. 9 illustrates the signal flows in an active beamforming frontend with passive mixer. Note that only one mixer switch and one baseband capacitor is shown for clarity.

The LNA transconductor converts the RF voltage into current i_{LNA} , which is mixed down by the mixer switch with a 25% duty cycle clock waveform. The downconverted modulated current i_{BB} has a conversion gain of $1/4 \text{sinc}(1/4) \approx 0.9$,

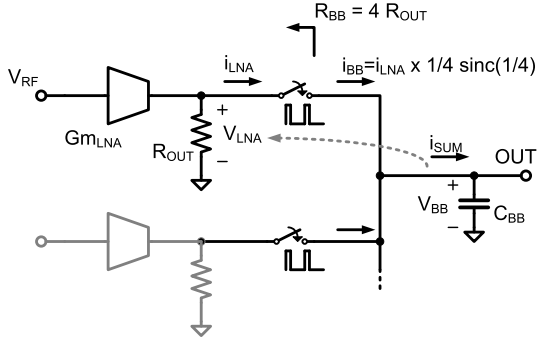


Fig. 9. Signal transformation in an active beamformer with passive mixer.

which models the conversion of RF current into higher mixer harmonics [18].

If only one frontend is present, the baseband current i_{BB} gets converted into voltage by the equivalent baseband impedance R_{BB} . This impedance is equivalent to four times the LNA output impedance, as it is connected by the switch to the baseband node for one-quarter of the time. The gain (in-beam and in-band) of the frontend is therefore equivalent to

$$G_{BB} = Gm_{LNA} \cdot R_{OUT} \cdot \text{sinc}(1/4) \quad (6)$$

which is the intrinsic voltage gain of the LNA inverter reduced by the mixer conversion loss of 0.9 dB.

A pole is present at the baseband node due to the equivalent baseband impedance R_{BB} and capacitor C_{BB} , with the frequency [21]

$$f_{BB} = \frac{1}{2\pi \cdot 4 \cdot R_{OUT} C_{BB}}. \quad (7)$$

From the impedance transformation properties of the passive mixer, the filtered baseband voltage gets upconverted to the LNA RF output node. This can be seen as a second mixer action, since the passive mixer is bidirectional. The conversion gain of this upconversion is equivalent to $\text{sinc}(1/4) \approx 0.9$. As a result, the low-pass filtering on the baseband node is translated into a bandpass filtering on the mixer RF input [8].

The intermodulation products due to weak nonlinearity in this design are mainly generated by the LNA, since the linearity of the passive mixer is very high and the gain of the LNA is rather low. These components arise due to the nonlinearity in the inverter transconductance and drain-voltage-swing-induced distortion. Since the voltage on the LNA output is upconverted from the filtered baseband output voltage, the distortion currents of the NMOS and PMOS output conductances are filtered as well. Therefore, an increase of input-referred third-order intercept point (IIP3) is expected out-of-band, but up to a certain point where the transconductance nonlinearity is dominating.

When the baseband currents are out of phase, complete or partial cancelling of the currents occurs and the baseband voltage swing is reduced. This is the main principle behind spatial filtering from the beamforming array. In addition, it can be concluded that the LNA output voltage swing is reduced as well, leading to an increase of IIP3. However, the intermodulation currents due to the LNA transconductance can also be reduced due to the beamforming action, as they can cancel in

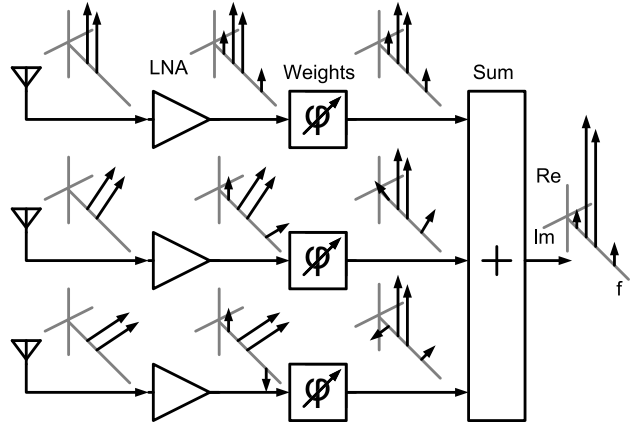


Fig. 10. Example of IM2 products in an active phased array.

the summation process. This depends on the relative phases of the intermodulation currents between antenna elements, as discussed in the next section.

B. Intermodulation Array Factor

The gain due to beamforming, the array factor AF, can be expressed as [22]

$$AF_{FUN}(u) = \sum_{n=0}^{N-1} e^{j2\pi \cdot n \frac{d}{\lambda} (u - u_0)} \quad (8)$$

where $u \equiv \sin(\theta)$ expresses the angle-of-arrival in u -space, d is the distance between the antenna elements, λ is the wavelength, u_0 is the direction in which the main beam is steered, and N is the number of antennas in the array. The array factor describes the spatial filtering that is performed by the array. For short-hand notation, we introduce the constant

$$\Phi \equiv 2\pi \frac{d}{\lambda}. \quad (9)$$

With the main beam steered to the signal of interest, interferers are spatially filtered by the array factor. By small perturbations of the element weights in both amplitude and phase, nulls can be steered to interferer directions, thereby maximizing interferer rejection [4].

Nonlinearity in the frontends before the summing node will generate intermodulation tones, which are affected by the beamforming as well. Fig. 10 illustrates the propagation of intermodulation tones in multiple antenna elements. The phase difference between fundamental tones of different antenna elements is preserved after the nonlinearity. As such, the intermodulation tones have defined phase differences depending on the particular intermodulation product, and are shaped by a different antenna factor than the fundamental tones.

In this analysis, we consider the distortion caused by two interferers with sinusoidal sources, with frequencies ω_1 and ω_2 , respectively, which are being received on angles u_1 and u_2 , respectively. The n th antenna will receive the following sum of the two phase-shifted interferers:

$$RX_n(t) = \cos(\omega_1 t + n \cdot u_1 \cdot \Phi) + \cos(\omega_2 t + n \cdot u_2 \cdot \Phi). \quad (10)$$

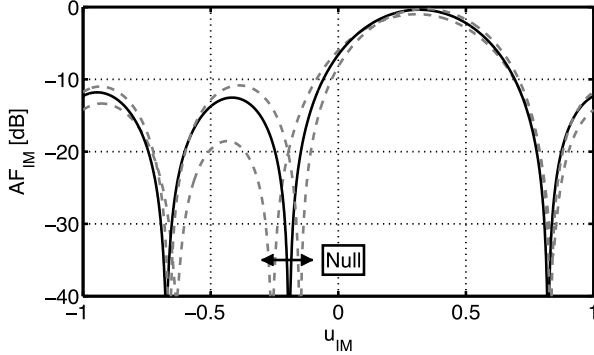


Fig. 11. Null steering in the intermodulation array factor AF_{IM} . Two alternative array factors with the null located in a different location are indicated by dashed lines.

The array is pointed toward the desired signal at angle u_0 so that its phase shift across the elements is equal in phase and the signal is coherently summed.

In contrast, after third-order distortion in the LNA, third-order intermodulation (IM3) terms emerge on the n th channel (RX_N)³(t)

$$\begin{aligned} &= C_{12} \cdot \cos((2 \cdot \omega_1 - \omega_2)t + n \cdot (2 \cdot u_1 - u_2)\Phi) \\ &\quad + C_{21} \cdot \cos((2 \cdot \omega_2 - \omega_1)t + n \cdot (2 \cdot u_2 - u_1)\Phi) + \dots \end{aligned} \quad (11)$$

where C_{12} and C_{21} are constants. In particular, an IM3 term emerges with the frequency $2 \cdot \omega_1 - \omega_2$ and a second term with $2 \cdot \omega_2 - \omega_1$. The phases of the IM3 terms are equal to $n \cdot (2 \cdot u_1 - u_2)\Phi$ and $n \cdot (2 \cdot u_2 - u_1)\Phi$, respectively. Comparing with (10), it is seen that these phase differences correspond to the case where a fundamental signal is originating from $2 \cdot u_2 - u_1$ and $2 \cdot u_1 - u_2$, respectively.

In general, we can conclude that for an intermodulation tone located at a frequency

$$\omega_{IM} = A_1 \cdot \omega_1 + A_2 \cdot \omega_2 \quad (12)$$

the corresponding effective angle in u-space of the intermodulation tone follows the same linear combination with coefficients A_1 and A_2 :

$$u_{IM} = A_1 \cdot u_1 + A_2 \cdot u_2. \quad (13)$$

By substitution into (8), the array factor for the intermodulation tone is equal to

$$AF_{IM} = \sum_{n=0}^{N-1} e^{jn\Phi(A_1u_1+A_2u_2-u_0)}. \quad (14)$$

Examining (14), it is seen that the intermodulation array factor AF_{IM} can be obtained from the fundamental array factor AF_{FUN} in (8) by the substitution of $u = u_{IM} = A_1 \cdot u_1 + A_2 \cdot u_2$. In principle, existing nulling algorithms that steer nulls in the fundamental array factor could also be used to steer nulls in the intermodulation array factor to improve linearity, as illustrated in Fig. 11. Fig. 11 plots an array factor by a solid line with a null located close to $u = 0.2$. This null can be steered to the location of an interferer by adjusting the beamforming weights. Two of these adjusted patterns

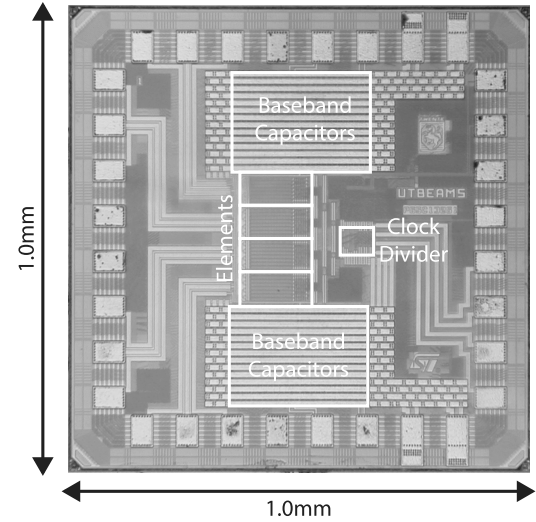


Fig. 12. Chip photograph of the four-element beamforming receiver, die measuring 1.0×1.0 mm.

with shifted null position are also displayed in Fig. 11 as dashed lines. For intermodulation nulling, it is, however, required to steer the null to the effective angle in u-space, u_{IM} , which is a combination of the angle of the interferers and the intermodulation coefficients, as outlined in (13). These algorithms are left for exploration in future work.

V. MEASUREMENTS

The four-element beamforming receiver was implemented in STMicroelectronics's standard 65-nm LP CMOS technology (die photograph in Fig. 12), with an active area of 0.20 mm^2 , including the baseband capacitors, RF ac coupling capacitors, and clock generation. The baseband switches and associated routing, which are additional requirements for a constant-Gm vector modulator, occupy less than 0.3% of the total active area. The baseband capacitance area is not affected by the slicing of the receiver elements and the RF ac decoupling capacitor area increases only by about 20%. This renders only a small change in the length of the required clock distribution wires and hence no significant additional power penalty.

A. Single-Element Measurements

The performance of a single element is evaluated by disabling all the reconfiguration switches in three out of four antenna elements. This effectively disconnects all but one antenna element from the output. The differential baseband outputs are sensed with two Lecroy AP033 high input impedance active differential probes. The frequency band of operation is from 1.0 to 2.5 GHz, with the center frequency set by the LO frequency. The baseband bandwidth can be changed from 30 to 300 MHz by the tunable baseband capacitances, allowing for operation in different radio standards.

The complete receiver frontend consumes between 26 to 36 mW from a 1 V supply, as the clock frequency is increased from 1.0 to 2.5 GHz. The increase in power consumption is due to the dynamic power consumed in the clock divider and clock tree. This amounts to 6.5 to 9 mW of power consumption per element, with clock generation included.

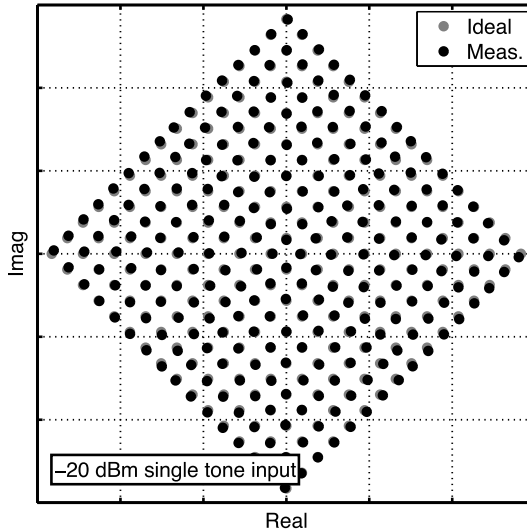


Fig. 13. Measured vector modulator constellation, single tone excitation with a -20 -dBm input power.

In the passband, the gain of a single element is measured to be 12 dB, with a Double Side Band (DSB) noise figure of 6 dB. With all four elements enabled, the baseband voltages of the elements are averaged, leading to the same baseband voltage swing as in the single element case in the main beam, where complete coherent summation occurs. The increased sensitivity is due to the reduced noise by the averaging (summing) operation, leading to a 6 -dB improvement for four elements.

The measured vector modulator constellation is given in Fig. 13 and compared with an ideal 16×16 square equidistance constellation. The constellation was measured with a vector network analyzer using a single-tone stimulus with an input power of -20 dBm. Note that this is not the modulation constellation of the signal, but the phase shifter constellation representing the possible phase shifts and amplitude adjustments that the vector modulator is capable of. The realized phasor points are close to the ideal, with an RMS phase error of 0.8° and an RMS gain error of 0.17 dB (Fig. 14). This translates into a 1.4% Error Vector Magnitude (EVM). The constellation of ten dies was measured and the mismatch between their constellations was determined to be 0.07 dB RMS in gain and 0.7° in phase. The high accuracy in the constellation is reached due to a small imbalance in the I/Q clocks and good matching between the vector modulator slices, without the need for calibration.

IIP3 and 1-dB CP are plotted for a clock frequency of 1.5 GHz in Fig. 15, together with the gain and S_{11} . It is observed that the IIP3 increases from 1 dBm in-band to 5 dBm out-of-band, while the CP increases from -9 dBm in-band to -3 dBm out-of-band. The increased linearity performance is due to the impedance transformation properties of the passive mixer in the vector modulator, which translates the lowpass baseband filter into an equivalent bandpass RF filter. This improves the robustness of this architecture to interferers present before the beamforming summing node. It can also be seen that the S_{11} is degraded out-of-band, due to the resistive-feedback matching network at the LNA input. Looking at Fig. 15, we see that a dip in 1-dB CP and

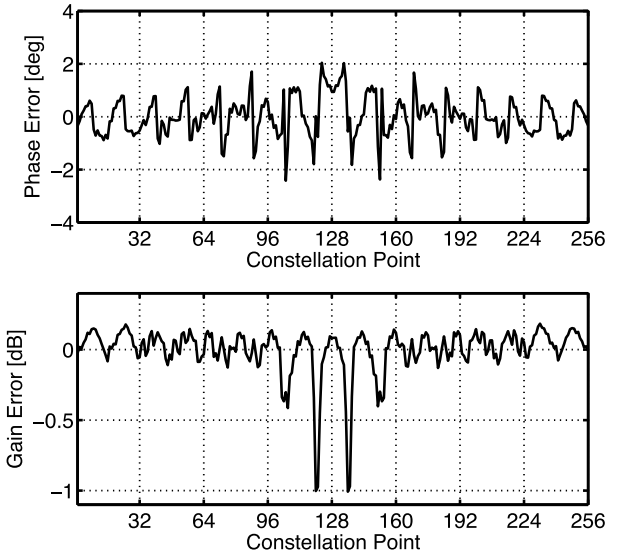


Fig. 14. Measured phase and gain errors of constellation.

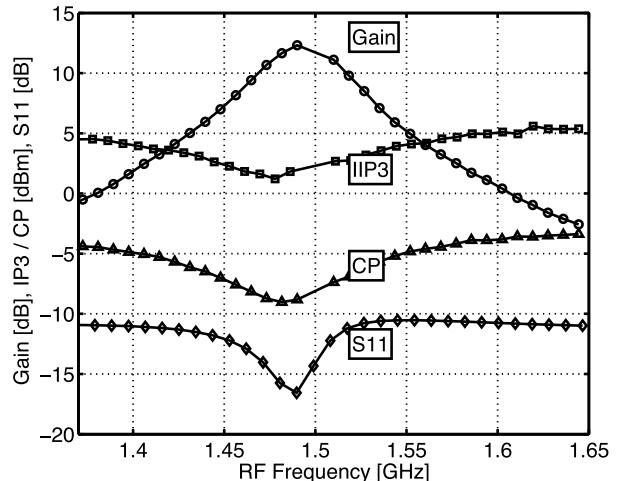


Fig. 15. Measured gain, linearity, and S_{11} at a 1.5 -GHz LO frequency for a single element.

IIP3 occurs at a frequency below the switching frequency of 1.5 GHz, which is likely related to the shift in S_{11} as often seen in N -path filters, due to parasitic input capacitance as discussed in [18]. It is notable that the maximum gain does not coincide exactly with these dips, which is a subject for further investigations.

Fig. 16 plots the gain, NF, and IIP3 over an LO frequency up to 2.5 GHz. The pole at the LNA output node is responsible for the gain roll-off at higher frequencies, limiting the maximum operating frequency of the receiver.

As interferers are present in the frontend up to the summing node, the small signal NF should not degrade when interferers are present. Fig. 17 plots the single-element NF versus blocker power at 1.5 GHz RF with an 80 -MHz blocker offset. The NF is unaffected up to -20 dBm of blocker power, after which a 3 -dB degradation is present at -10 dBm of blocker power.

B. Intermodulation Array Factor

In these measurements, the IIP3 of the beamforming receiver is measured and compared with the theoretical

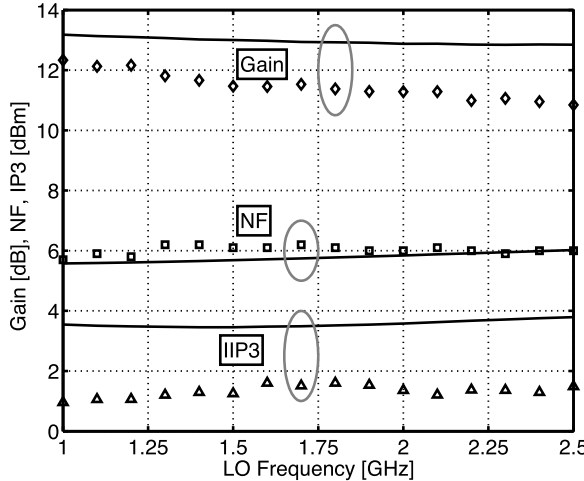


Fig. 16. Gain, NF, and IIP3 swept over LO frequency for a single element (simulation shown by lines and measurements by markers).

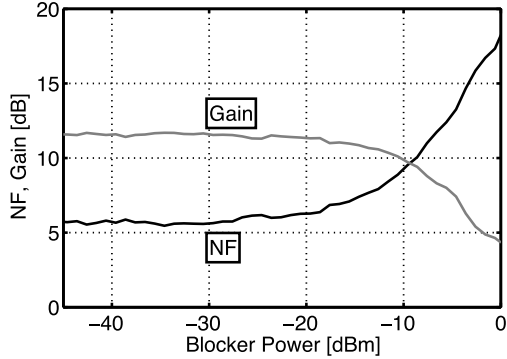


Fig. 17. Measured single-element noise figure versus blocker power.

intermodulation array factor equations, as discussed in the previous section. Three somewhat arbitrary cases will be discussed that exhibit interesting behavior and show the merit of the intermodulation array factor for predicting the linearity performance of the beamforming receiver.

To this end, the intermodulation distortion performance of the beamforming phased array was evaluated with the measurement setup in Fig. 18. An RF signal is split into four and phase shifted with high-precision discrete vector modulators (Telemakus TEV2700-45) to emulate an interferer wavefront coming from direction u_1 . At the same time, a second RF signal is split into four and fed directly into the receiver, thereby emulating a second interferer coming from broadside ($u_2 = 0$). In addition, the receiver applies the required phase shift to point the main beam to the desired signal direction u_0 (in this experiment, no amplitude control is utilized to steer the nulls). In this setup, we can therefore control the angle between the two interferers and the angle between the main beam and the interferers.

Care was taken to match transmission lines and power splitter/combiners in this setup, in order to minimize the effect of phase and gain errors on the measurement results. The external vector modulators were individually calibrated. We estimate that the resulting phase and gain errors were less than 1.0° and 0.1 dB, respectively, which if modeled as random errors in a four-element phased array would result in a peak error sidelobe level of better than 28 dB below

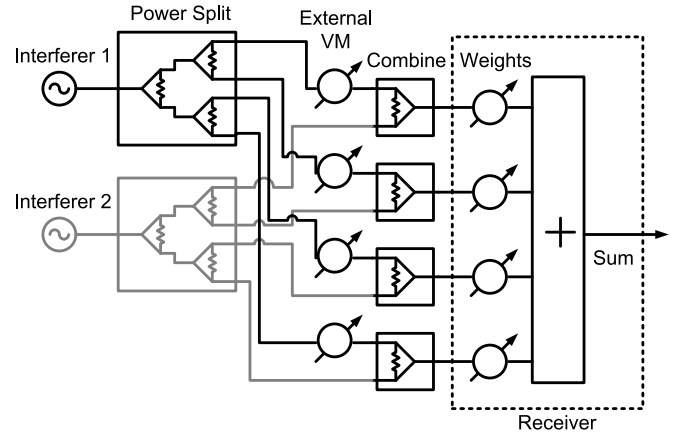


Fig. 18. Intermodulation measurement setup.

the main beam [23]. As the nulls in the measured IIP3 are less than 20 dB deep and are at the same location as the nulls in the simulated intermodulation beamforming array factor, we therefore believe that this measurement setup has adequately low phase and gain errors.

With a spectrum analyzer, the fundamental and IM3 products after summing were measured and an IIP3 was calculated. We will now show that the IIP3 depends on the angles between the main beam and the two interferers. To illustrate this point, Fig. 19 plots the IIP3 calculated from the IM3 frequency tone ($A_1 = 2$ and $A_2 = -1$) for three scenarios. The calculated intermodulation array factor according to (14) is displayed in gray. In the first scenario shown in Fig. 19(a), the two interferers are located at the same angle. In this case, $u_1 = u_2$ and the intermodulation array factor is calculated as

$$\begin{aligned} \text{AF}_{\text{IM}}(u_1 - u_0)|_{u_1=u_2} &= \sum_{n=0}^{N-1} e^{jn\Phi(2*u_1 - u_2 - u_0)} \\ &= \sum_{n=0}^{N-1} e^{jn\Phi(u_1 - u_0)} = \text{AF}_{\text{FUN}}(u = u_1 - u_0). \end{aligned} \quad (15)$$

In this case, when the two interferer tones are at the same angle, the IM3 AF follows the fundamental tone AF. It is observed that the IIP3 is increased when the array factor is decreased by as much as 18 dB. When the interferers are at the same direction as the main beam, the IIP3 is minimum as no cancellation is possible without reducing the desired signal as well.

In the second scenario in Fig. 19(b), the interferers are spaced apart by 45° (0.5 in u-space) and their direction is swept with respect to the main beam. In this case, $u_2 = u_1 + 0.5$, and we can derive

$$\begin{aligned} \text{AF}_{\text{IM}}(u_1 - u_0)|_{u_2=u_1+0.5} &= \sum_{n=0}^{N-1} e^{jn\Phi(2*u_1 - u_2 - u_0)} \\ &= \sum_{n=0}^{N-1} e^{jn\Phi(u_1 - u_0 - (u_1 - u_2))} \\ &= \text{AF}_{\text{FUN}}(u = u_1 - u_0 - 0.5). \end{aligned} \quad (16)$$

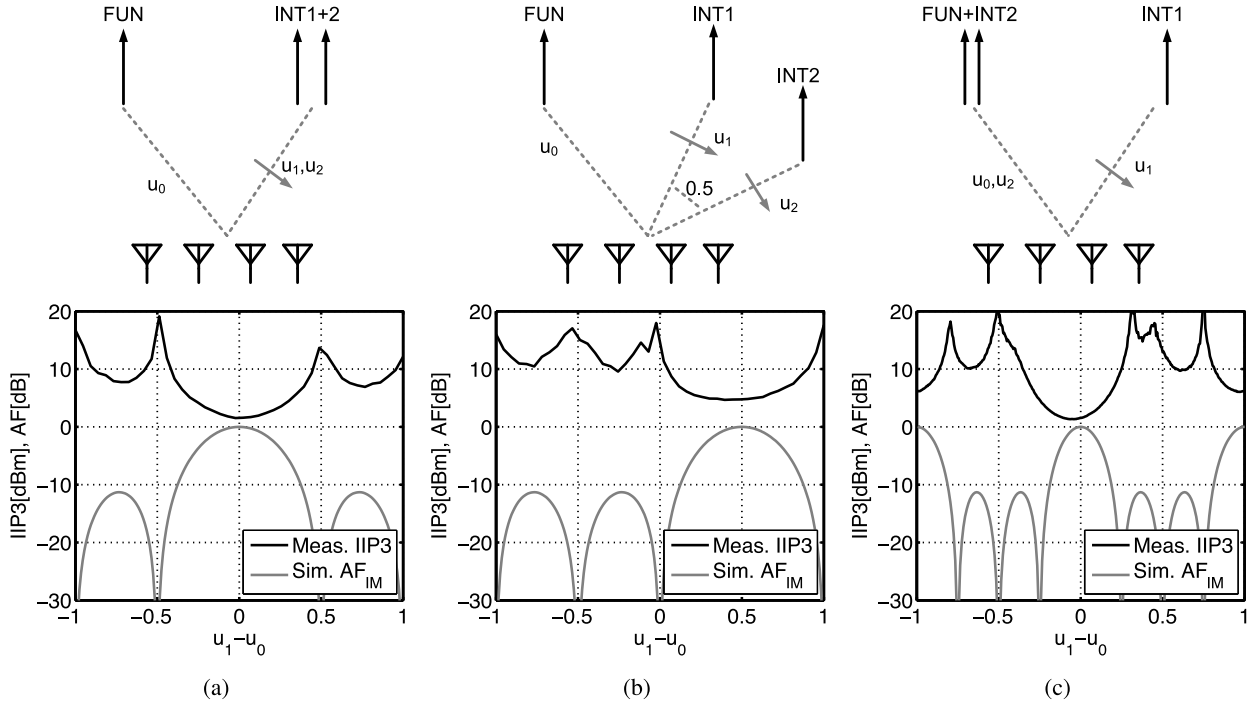


Fig. 19. Calculated IM3 array factors (AF_{IM}) and measured IIP3 for (a) $u_1 = u_2$, (b) $u_2 = u_1 + 0.5$, and (c) $u_2 = u_0$.

This means that the intermodulation AF is shifted with respect to the fundamental AF (by 0.5 in u-space). Interestingly, even when one interferer is at the same angle as the main beam ($u_1 - u_0 = 0$), cancelling of its intermodulation product is achieved by the second interferer at angle $u_2 = u_0 + 0.5$.

In the third scenario, Fig. 19(c) displays the scenario when one interferer is kept with the same direction as the main beam, while the second interferer is swept so that $u_2 = u_0$.

$$\begin{aligned} \text{AF}_{\text{IM}}(u_1 - u_0)|_{u_2=u_0} &= \sum_{n=0}^{N-1} e^{jn\Phi(2u_1 - u_2 - u_0)} \\ &= \sum_{n=0}^{N-1} e^{jn\Phi(2u_1 - 2u_0)} \\ &= \text{AF}_{\text{FUN}}(u = 2(u_1 - u_0)). \end{aligned} \quad (17)$$

In this case, the intermodulation array factor in u-space is compressed by a factor of two compared with the fundamental array factor. With the first interferer at angle $u_1 = 1.0$, the fundamental AF would suggest a high IIP3, but the IM3 AF reveals that the intermodulation products are not cancelled and the measurement reveals a low IIP3 instead.

Since the receiver is capable of both amplitude and phase steering, an adaptive nulling algorithm could be used to steer the nulls in the intermodulation AF to the angle of the interferers, depending on the actual interferer scenario. The details of this implementation are left as future work.

C. Comparison With State-of-the-Art Beamforming Receivers

The measured results are compared with state-of-the-art beamforming receivers in Table I. This design consumes between 6.5 and 9.0 mW of power per element, while achieving an NF of 6 dB, which is significantly lower power

consumption than the state-of-the-art measurements. This is achieved by utilizing the following design techniques. First, the constant-Gm vector modulator architecture efficiently utilizes a fixed number of transconductances to produce each point on the constellation. This architecture furthermore allows the transconductances to be moved from baseband to RF, which achieves a fourfold reduction of the total required transconductance. Note that the LO phase generation is included in the power consumption of all designs by dividing its power dissipation by the number of elements.

In earlier published designs, a multitude of linearity performance figures has been reported, due to the combination of frequency and spatial filtering in beamforming receivers. Similar to the familiar in-band and out-of-band distortion figures, which define whether we are inside or outside the frequency filtered band of interest, we can define in-beam as the condition where maximal coherent summing occurs and out-of-beam where some spatial filtering occurs.

As some designs do not provide gain [6]–[8], using the input-referred IP3 under in-beam conditions can be misleading as linearity will be degraded by subsequent gain stages. In this case, comparing the output-referred IP3 is preferred. On the other hand, out-of-beam conditions justify that spatial filtering has occurred and that the interferers are suppressed sufficiently such that additional gain stages do not degrade linearity further, enabling the use of input-referred IP3. This design achieves a high in-band IP3 due to the spatial suppression of intermodulation products, while the out-of-band IIP3 is limited by the input transconductor and is lower than passive-first designs with N-path filters applied to the RF input [6]–[8] or across the input transconductor [9].

There is a tradeoff between RF frequency and power consumption in this architecture. The RF frequency range is

TABLE I
COMPARISON WITH STATE-OF-THE-ART BEAMFORMING RECEIVERS

	[3]	[6]	[7]	[8]	[9]	This Work	
Technology	90nm	65nm	65nm	28nm	65nm	65nm	
Active Area	1.4	0.18	0.97	0.65	1.69	0.20	mm ²
Supply Voltage	1.2	1.0-1.2	1.2	1.0	1.2	1.0	V
RF Frequency	4.0	1.5-5.0	0.6-3.6	0.6-4.5	0.1-1.7	1.0-2.5	GHz
Power/Element	41 [†]	16-42 [†]	17-49 [†]	8.5-30 [†]	37@500MHz [†]	6.5-9 [†]	mW
# Phase Shifter Steps	32	32	8	8	64	44	
Gain	15	-6	-1	-1	41	12	dB
1-Element Noise Figure	13	18	4	4	2.2-4.6	6	dB
4-Element SNR improvement	6	6	4	4	6	6	dB
CP (in-band,in-beam)	N/A	2	-5	-5.5	N/A	-9	dBm
OIP3 (in-band,in-beam)	17	7	5	5	0	13	dBm
IIP3 (in-band,out-of-beam)	N/A	N/A	+2..+9	+5.5..+11	-7	+1..+20	dBm
IIP3 (out-of-band,in-beam)	+2	N/A	+11	+20	+11	+5	dBm

[†] Includes LO clock divider power divided by the number of elements.

mainly limited by two effects, namely, the pole at the LNA output node and parasitic capacitance in the LO frequency divider. In the current design, the LNA output capacitance dominates the bandwidth limitation, which is largely determined by the intrinsic speed of the technology but can be improved by increasing the supply voltage. Even though the clock divider is implemented using power-efficient dynamic logic, it becomes a relevant power contribution at high frequency, as power consumption scales linearly with frequency. Reducing the mixer switch size helps to reduce the capacitive loading to the LO frequency divider, but comes at the cost of less out-of-band N -path filtering and hence degrades out-of-band and out-of-beam linearity.

From the comparison, we can conclude that this design achieves a balance among the NF, gain, and intermodulation distortion performances, while maintaining low power consumption.

VI. CONCLUSION

In this paper, a low-power four-element beamforming receiver with a constant-Gm vector modulator was presented. The vector modulator combines the rotated binary scaled signals into the phase shifted and amplitude scaled output, implementing a 16×16 square constellation. The constant number of enabled transconductances avoids errors due to code-dependent loading of the circuit nodes. By moving the vector modulator transconductors into the RF domain before the passive 25% duty cycle I/Q mixer, a fourfold reduction in the amount of transconductance is achieved. The shunt resistor feedback inverter-based transconductors double as the LNA and provide low-power impedance matching at the input ports.

The 65-nm implementation consumes between 6.5 and 9 mW per antenna element in the 1.0–2.5-GHz RF frequency band, including clock generator, and achieves a single-element 6-dB NF. The measured RMS phase and gain errors with respect to an ideal square equidistance constellation are 0.8° and 0.17 dB, respectively. A theoretical model for the cancellation of frontend intermodulation products in active phased arrays was given, showing that these products follow a different array factor due to their modified effective angle

of arrival. The measurements observed an improvement of up to 19 dB in the IIP3 for out-of-beam interferers.

ACKNOWLEDGMENT

The authors would like to thank STMicroelectronics for the silicon donation and CMP for the assistance, H. Westerveld for the assistance during the measurements, and G. Wienk and H. de Vries for the CAD support and the laboratory assistance.

REFERENCES

- [1] J. Paramesh, R. Bishop, K. Soumyanath, and D. J. Allstot, “A 1.4V 5GHz four-antenna Cartesian-combining receiver in 90nm CMOS for beamforming and spatial diversity applications,” in *IEEE ISSCC Dig. Tech. Papers*, vol. 1, Feb. 2005, pp. 210–211.
- [2] S. Kundu and J. Paramesh, “A compact, supply-voltage scalable 45–66 GHz baseband-combining CMOS phased-array receiver.” *IEEE J. Solid-State Circuits*, vol. 50, no. 2, pp. 527–542, Feb. 2015.
- [3] R. Tseng, H. Li, D. H. Kwon, Y. Chiu, and A. S. Y. Poon, “A four-channel beamforming down-converter in 90-nm CMOS utilizing phase-oversampling.” *IEEE J. Solid-State Circuits*, vol. 45, no. 11, pp. 2262–2272, Nov. 2010.
- [4] M. C. M. Soer, E. A. M. Klumperink, B. Nauta, and F. E. van Vliet, “Spatial interferer rejection in a four-element beamforming receiver front-end with a switched-capacitor vector modulator,” *IEEE J. Solid-State Circuits*, vol. 46, no. 12, pp. 2933–2942, Dec. 2011.
- [5] M. C. M. Soer, E. A. M. Klumperink, B. Nauta, and F. E. van Vliet, “A 1.0-to-4.0GHz 65nm CMOS four-Element beamforming receiver using a switched-capacitor vector modulator with approximate sine weighting via charge redistribution,” in *IEEE ISSCC Dig. Tech. Papers*, Feb. 2011, pp. 64–65.
- [6] M. C. M. Soer, E. A. M. Klumperink, B. Nauta, and F. E. van Vliet, “A 1.5-to-5.0GHz input-matched +2dBm P1dB all-passive switched-capacitor beamforming receiver front-end in 65nm CMOS,” in *IEEE ISSCC Dig. Tech. Papers*, Feb. 2012, pp. 174–175.
- [7] A. Ghaffari, E. A. M. Klumperink, F. E. van Vliet, and B. Nauta, “Simultaneous spatial and frequency-domain filtering at the antenna inputs achieving up to +10dBm out-of-band/beam P1dB,” in *IEEE ISSCC Dig. Tech. Papers*, Feb. 2013, pp. 84–85.
- [8] A. Ghaffari, E. A. M. Klumperink, F. E. van Vliet, and B. Nauta, “A 4-element phased-array system with simultaneous spatial- and frequency-domain filtering at the antenna inputs,” *IEEE J. Solid-State Circuits*, vol. 49, no. 6, pp. 1303–1316, Jun. 2014.
- [9] L. Zhang, A. Natarajan, and H. Krishnaswamy, “A scalable 0.1-to-1.7GHz spatio-spectral-filtering 4-element MIMO receiver array with spatial notch suppression enabling digital beamforming,” in *IEEE Int. Solid-State Circuits Conf. (ISSCC) Dig. Tech. Papers*, Jan. 2016, pp. 166–167.

- [10] M. C. M. Soer, E. A. M. Klumperink, B. Nauta, and F. E. van Vliet, "A 1.0-to-2.5GHz beamforming receiver with constant-Gm vector modulator consuming < 9mW per antenna element in 65nm CMOS," in *IEEE ISSCC Dig. Tech. Papers*, Feb. 2014, pp. 66–67.
- [11] H. Krishnaswamy and L. Zhang, "Analog and RF interference mitigation for integrated MIMO receiver arrays," *Proc. IEEE*, vol. 104, no. 3, pp. 561–575, Mar. 2016.
- [12] K.-J. Koh and G. M. Rebeiz, "0.13- μ m CMOS phase shifters for X-, Ku-, and K-band phased arrays," *IEEE J. Solid-State Circuits*, vol. 42, no. 11, pp. 2535–2546, Nov. 2007.
- [13] K.-J. Koh and G. M. Rebeiz, "An X- and Ku-band 8-element phased-array receiver in 0.18- μ m SiGe BiCMOS technology," *IEEE J. Solid-State Circuits*, vol. 43, no. 6, pp. 1360–1371, Jun. 2008.
- [14] M. C. M. Soer, E. A. M. Klumperink, P.-T. de Boer, F. E. van Vliet, and B. Nauta, "Unified frequency-domain analysis of switched-series-RC passive mixers and samplers," *IEEE Trans. Circuits Syst. I, Reg. Papers*, vol. 57, no. 10, pp. 2618–2631, Oct. 2010.
- [15] D. Murphy *et al.*, "A blocker-tolerant wideband noise-cancelling receiver with a 2dB noise figure," in *IEEE ISSCC Dig. Tech. Papers*, Feb. 2012, pp. 74–75.
- [16] S. B. T. Wang, A. M. Niknejad, and R. W. Brodersen, "Design of a sub-mW 960-MHz UWB CMOS LNA," *IEEE J. Solid-State Circuits*, vol. 41, no. 11, pp. 2449–2456, Nov. 2006.
- [17] B. van Liempd *et al.*, "A 0.9 V 0.4–6 GHz harmonic recombination SDR receiver in 28 nm CMOS with HR3/HR5 and IIP2 calibration," *IEEE J. Solid-State Circuits*, vol. 49, no. 8, pp. 1815–1826, Aug. 2014.
- [18] C. Andrews and A. C. Molnar, "Implications of passive mixer transparency for impedance matching and noise figure in passive mixer-first receivers," *IEEE Trans. Circuits Syst. I, Reg. Papers*, vol. 57, no. 12, pp. 3092–3103, Dec. 2010.
- [19] A. Mirzaei, H. Darabi, and D. Murphy, "Architectural evolution of integrated M-phase high-Q bandpass filters," *IEEE Trans. Circuits Syst. I, Reg. Papers*, vol. 59, no. 1, pp. 52–65, Jan. 2012.
- [20] J. Borremans *et al.*, "A 40 nm CMOS 0.4–6 GHz receiver resilient to out-of-band blockers," *IEEE J. Solid-State Circuits*, vol. 46, no. 7, pp. 1659–1671, Jul. 2011.
- [21] M. C. M. Soer, E. A. M. Klumperink, Z. Ru, F. E. van Vliet, and B. Nauta, "A 0.2-to-2.0GHz 65nm CMOS receiver without LNA achieving >11dBm IIP3 and <6.5 dB NF," in *IEEE ISSCC Dig. Tech. Papers*, vol. 52, Feb. 2009, pp. 222–223.
- [22] C. A. Balanis, *Antenna Theory, Analysis and Design*. New York, NY, USA: Wiley, 2005.
- [23] J. L. Allen, "The theory of array antennas," MIT Lincoln Lab., Lexington, MA, USA, Tech. Rep. 323, 1963.



Michiel C. M. Soer was born in Schoonhoven, The Netherlands, in 1984. He received the M.Sc. (*cum laude*) degree in electrical engineering and the Ph.D. (*cum laude*) degree from the University of Twente, Enschede, The Netherlands, in 2007 and 2012, respectively.

He is currently with Spark Microsystems, Montreal, QC, Canada. His current research interests include mixers, discrete time systems, phased arrays, and ultralow-power impulse radios in CMOS.



Eric A. M. Klumperink (M'98–SM'06) was born in Lichtenvoorde, The Netherlands, in 1960. He received the B.Sc. degree in electrical engineering from Hogere Technische School, Enschede, The Netherlands, in 1982, and the Ph.D. degree from the University of Twente, Enschede, in 1997.

He joined the University of Twente in 1984. In 1998, he was an Assistant Professor with the IC Design Laboratory, Twente, The Netherlands. He has authored or co-authored more than 150 internationally refereed journal and conference papers, and was recognized as the contributor of more than 20 ISSCC papers during 1954–2013, and holds more than ten patents.

Dr. Klumperink is a member of the Technical Program Committees of the ISSCC and the IEEE RFIC Symposium. He was a co-recipient of the ISSCC 2002 and the ISSCC 2009 Van Vessem Outstanding Paper Award. He served as an Associate Editor of the IEEE TRANSACTIONS ON CIRCUITS AND SYSTEM (TCAS)-II during 2006–2007, the IEEE TCAS-I during 2008–2009, and the IEEE JOURNAL OF SOLID-STATE CIRCUITS (JSSC) during 2010–2014. He served as an IEEE SSC Distinguished Lecturer in 2014–2015.



Dirk-Jan van den Broek was born in Roosendaal, The Netherlands, in 1986. He received the M.Sc. (*cum laude*) degree in electrical engineering from the University of Twente, Enschede, The Netherlands, in 2012, where he is currently pursuing the Ph.D. degree with the ICD-Group, investigating full-duplex CMOS front-end techniques.



Bram Nauta (M'91–SM'03–F'08) was born in Hengelo, The Netherlands, in 1964. He received the M.Sc. (*cum laude*) degree in electrical engineering and the Ph.D. degree with a specialization in analog CMOS filters for very high frequencies from the University of Twente, Enschede, The Netherlands, in 1987 and 1991, respectively.

In 1991, he joined the Mixed-Signal Circuits and Systems Department, Philips Research, Eindhoven, The Netherlands. In 1998, he joined the University of Twente, where he is currently a Distinguished Professor and the Head of the IC Design Group. His current research interests include high-speed analog CMOS circuits, software defined radio, cognitive radio, and beamforming.

Dr. Nauta was in the Technical Program Committee of the Symposium on very large scale integration circuits during 2009–2013, and is in the Steering Committee and Programme Committee of the European Solid State Circuit Conference. He was a co-recipient of the International Solid State Circuits Conference (ISSCC) 2002 and 2009 "Van Vessem Outstanding Paper Award," the Simon Stevin Meester Award (500,000) in 2014, and the largest Dutch National Prize for achievements in technical sciences. He served as a Distinguished Lecturer of the IEEE. He served as the Editor-in-Chief of the IEEE JOURNAL OF SOLID-STATE CIRCUITS (JSSC) during 2007–2010, and the 2013 Program Chair of ISSCC. He is currently the Vice President of the IEEE Solid-State Circuits Society and also served as an Associate Editor of the IEEE TRANSACTIONS ON CIRCUITS AND SYSTEMS II during 1997–1999, and of JSSC during 2001–2006.



Frank E. van Vliet (M'95–SM'06) was born in Dubbeldam, The Netherlands, in 1969. He received the M.Sc. (with Hons.) degree in electrical engineering and the Ph.D. degree in monolithic microwave integrated circuit (MMIC) filters from the Delft University of Technology, Delft, The Netherlands, in 1997.

He joined TNO, Den Haag, The Netherlands (Netherlands Organisation for Applied Scientific Research) in 1997, where he is currently a Principal Scientist responsible for MMIC, antenna, and transmit/receive module research. In 2007, he joined the Integrated Circuit Design Group, University of Twente, Enschede, The Netherlands, as a Professor of Microwave Integration, where he founded the Centre for Array Technology. He has co-authored over 100 peer-reviewed publications. His current research interests include MMICs in all their aspects, advanced measurement techniques, and phased-array technology.

Dr. Vliet is a member of the European Space Agencies, Component Technology Board for microwave components, and the European Defence Agencies CapTech IAP-01. He was the Chair of the 2012 European Microwave Integrated Circuit conference (EuMIC), and founded the Doctoral School of Microwaves. He serves on the TPC of EuMIC, the IEEE International Symposium on Phased Array Systems and Technology, the IEEE Compound Semiconductor IC Symposium, and the IEEE Conference on Microwaves, Communications, Antennas, and Electronic Systems. He is a Guest Editor of the IEEE TRANSACTIONS ON MICROWAVE THEORY AND TECHNIQUES 2013 Special Issue on Phased-Array Technology.